



PsLSNet: Automated psoriasis skin lesion segmentation using modified U-Net-based fully convolutional network



Manoranjan Dash^a, Narendra D. Londhe^{a,*}, Subhojit Ghosh^a, Ashish Semwal^a, Rajendra S. Sonawane^b

^a Electrical Engineering Department, National Institute of Technology, Raipur, India

^b Psoriasis Clinic and Research Centre, Psoriatreat, Pune, Maharashtra, India

ARTICLE INFO

Article history:

Received 2 November 2018

Received in revised form 12 February 2019

Accepted 6 April 2019

Available online 8 May 2019

Keywords:

Psoriasis

Segmentation

Fully convolutional network

U-Net

Deep learning

ABSTRACT

The segmentation of psoriasis skin lesions from RGB color images is a challenging task in the computer vision, due to poor illumination conditions, the irregular shapes and sizes of psoriasis lesions, fuzzy boundaries between the lesions and the surrounding skin, and various artifacts such as skin hairs and camera reflections. The manual segmentation of lesions is very time-consuming and laborious for the dermatologist, and various automatic lesion segmentation approaches have therefore been presented by researchers in the recent past. However, these existing state-of-the-art approaches have various limitations, such as being highly dependent on feature engineering, showing poor performance in terms of accuracy and failing to consider challenging cases, as explained above. In view of this, we present an automated psoriasis lesion segmentation method based on a modified U-Net architecture, referred as PsLSNet. The architecture consists of a 29-layer deep fully convolutional network, for extracting spatial information automatically. In U-Net architecture there are two paths namely contracting and extracting, which are connected as U-shape. The proposed convolutional neural network also provides accelerated training by reducing the covariate shift through the implementation of batch normalization and is capable of segmenting the lesion even in challenging cases such as under poor acquisition conditions and in the presence of artifacts. In our experiment, we use 5241 images of psoriasis lesions collected from 1026 psoriasis patients by a dermatologist. The experimental results show effective performance metrics such as a Dice coefficient of 93.03% and an accuracy of 94.80%, with 89.60% sensitivity and 97.60% specificity, values that are significantly higher than for existing approaches.

© 2019 Elsevier Ltd. All rights reserved.

1. Introduction

Psoriasis is a type of skin disease that may affect parts or the whole of the body, regardless of gender and age [1]. Most researchers and dermatologists report that genomics is the main cause of psoriasis [2], in which the skin grows faster and for a longer period compared to normal skin [3]. This also affects the social life of patients, who feel very uncomfortable and embarrassed due to the continuous itching and ugly physical appearance [4]. Statistics show that approximately 3% of the global population is affected by this disease in various geographical zones [5]. There are several forms of the appearance of psoriasis on the skin, such

as plaque, guttate, inverse, pustular and erythrodermic formations [6], and of these, the plaque is the most commonly found [7,8]. This disease requires a periodic and effective treatment. Currently, subjective assessment (by visual inspection and sense of touch) is the most widely adopted treatment procedure by dermatologists, in which the segmentation of the psoriasis lesion is a primary step in assessing the disease. However, this subjective manual assessment is a difficult, time-consuming task that depends entirely on the experience and/or expertise of the dermatologist [9]. Hence, a computer-aided diagnosis (CAD) system for the development of a fast, effective treatment and objective assessment would be a desirable eventual solution for automatically segmenting the psoriasis lesions.

In view of this, several works [10–17] have been reported with regard to the detection of psoriasis lesions since the early 2000s. Taur et al. [10,11] applied a multi-resolution-based signature subspace classifier (MSSC) and a neuro-fuzzy classifier to segment lesions in three psoriasis images, and the performance of these

* Corresponding author at: National Institute of Technology, Raipur, India.

E-mail addresses: manoranjandash324@gmail.com (M. Dash), nlondhe.ele@nitrr.ac.in (N.D. Londhe), sghosh.ele@nitrr.ac (S. Ghosh), ashish.semwal92@gmail.com (A. Semwal), drrajss@gmail.com (R.S. Sonawane).

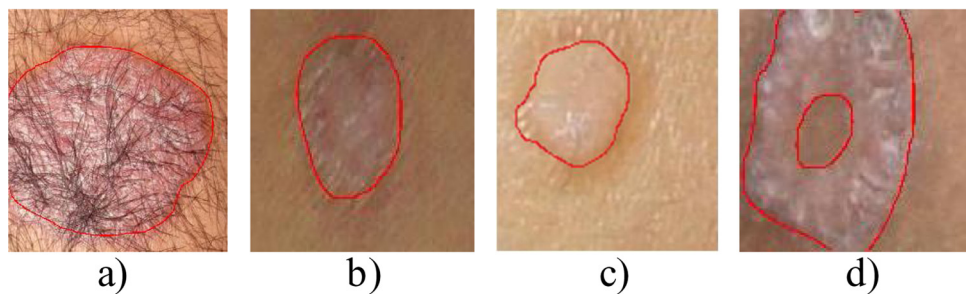


Fig. 1. Challenges in the automated segmentation of skin lesions in psoriasis images: (a) hair artefacts; (b) low contrast and a fuzzy boundary between the lesion and the surrounding skin; (c) the very similar appearance of a psoriasis lesion and the surrounding skin; and (d) normal skin located in the middle of psoriasis lesion. The red contour indicates skin lesions contoured by dermatologists.

approaches was evaluated based on visual presentation and accuracy, respectively. Following this, Nidhal et al. [12] used a neural network (NN)-based segmentation algorithm for 24 images of psoriasis and other diseases, and evaluated the performance based on accuracy alone. A technique for psoriasis lesion detection based on K-means for a maximum data size of five was presented by Li-Hong et al. [13], for which an accuracy of 91.58% was found. A year later, geometric active contours were employed for the segmentation of 24 images of psoriasis by Bogo et al. [14], and the results were visually interpreted to evaluate performance. In 2013, a method for the detection of lesions in 282 psoriasis images using a Gaussian mixture model (GMM) was proposed and visually evaluated by Guoli et al. [15]. A technique combining a Markov random field (MRF) and a support vector machine (SVM) was applied to 103 psoriasis images by Lu et al. [16] to segment lesions, and this achieved a Dice coefficient of 0.5503, a sensitivity of 0.8179, and a specificity of 0.8707. Furthermore, Shrivastava et al. [17] conducted psoriasis lesion detection for a maximum data size of 100 using a K-means technique and morphological post-processing. The performance of this segmentation method was validated using visual depiction [10,14,15], accuracy metrics [11–13] and the Dice coefficient metric [16]. However, these studies were carried out with a smaller amount of data and the performance evaluation was based on only the accuracy, the Dice coefficient, and visual assessments. The automatic segmentation of lesions in psoriasis images is a challenging task in such a small dataset, due to aspects such as: (a) hair artefacts; (b) low levels of contrast and fuzzy boundaries between the lesion and the surrounding skin; (c) the almost similar appearance of a psoriasis lesion and surrounding skin; and (d) normal skin located in the middle of a psoriasis lesion [18], as shown in Fig. 1.

In this context, our team recently attempted automatic segmentation using a feature-based Bayesian framework [19] to detect psoriasis lesions using a larger dataset of 670 images. The Dice coefficient was increased to 0.82 by adopting different 172 color features and feature selection techniques in order to retain the best features. However, this feature-based Bayesian framework relies heavily on the best features to define the posterior probability for the classification of each pixel into skin and lesion, which is a time-consuming process. Various other methods [10–16] have been employed to segment the region of interest from medical images, some of which utilize classical machine learning approaches such as SVM, random forest (RF) etc. The extraction of handcraft features is essential in order to segment the region of interest prior to training the machine learning model. However, these feature engineering techniques fail to retain the spatial resolution of the image, which increases negative detection in challenging cases, as shown in Fig. 1. In recent years, deep learning approaches have been found to be the most promising and successful approaches to image segmentation in the biomedical domain [20,21].

These networks have been used to solve several practical classification challenges [22] and to give state-of-the-art results

compared to conventional machine learning methods such as SVM, RF etc. Convolutional network (CNN)-based approaches have shown tremendous success in image classification, as they have the ability to learn features automatically from the input data and perform classification tasks [20]. In addition to classification, CNNs have also recently been used to segment the brain in magnetic resonance imaging (MRI) [23], dermoscopic images (melanoma) [24], tumors in computed tomography (CT) images [25] and anatomical organs in chest radiographs [26]. Although a CNN has the ability to learn hierarchical features automatically from the input data and perform a classification task [20], the fully connected layer of the CNN is not suitable for dense predictions, as it does not provide spatial information at the output, which is important in dense prediction (pixel level prediction). In view of this, the fully connected layer of convolutional networks is replaced by a convolutional kernel (filter), which can process the entire image in order to preserve the spatial information and perform dense prediction [27,28].

In this paper, we propose a convolutional network that utilizes a U-Net [29] architecture for the detection of psoriasis lesions. This U-Net-based fully convolutional network (FCN) is employed to execute the pixel level classification (semantic segment), which separates the psoriasis lesion from healthy skin. A U-Net-based architecture can also segment the challenging images shown in Fig. 1 by extracting high-resolution features and can provide optimum segmentation results [29] even for a smaller training dataset.

The organization of this paper is as follows: in Section II, the architectural details of the proposed U-Net-based segmentation are introduced. In Section III, we present our experimental setup. The results and a discussion of the proposed method are presented in Sections IV and V, respectively.

2. PsLSNet for segmentation of psoriasis lesions

2.1. Overview of U-Net architecture

Fig. 2 represents the implemented FCN based on U-Net architecture for the segmentation of psoriasis skin lesions. A subsequent probability map of the input psoriasis image was obtained by training the architecture shown in Fig. 2. The original U-Net topology from [29] is modified here to achieve efficient training results for our application. The implemented architecture has two segments, a contracting path (left side) and an expanding path (right side), which are connected in a U shape, as shown in Fig. 3. Unlike the original U-Net topology, the contracting path in the proposed architecture utilizes 19 convolutional layers in conjunction with batch normalization and a ReLU activation function, followed by max pooling, as shown in Table 1. The max pooling operation was performed after every two convolution operations in the contracting path. The depth of the feature map is also doubled after every max pooling operation in order to learn the more representative

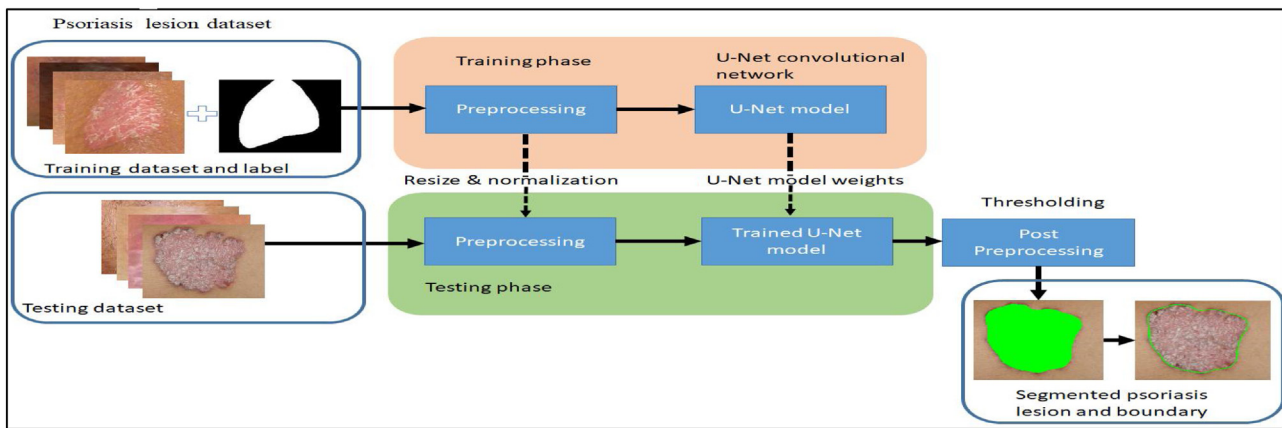


Fig. 2. Overview of the proposed method of psoriasis lesion segmentation.

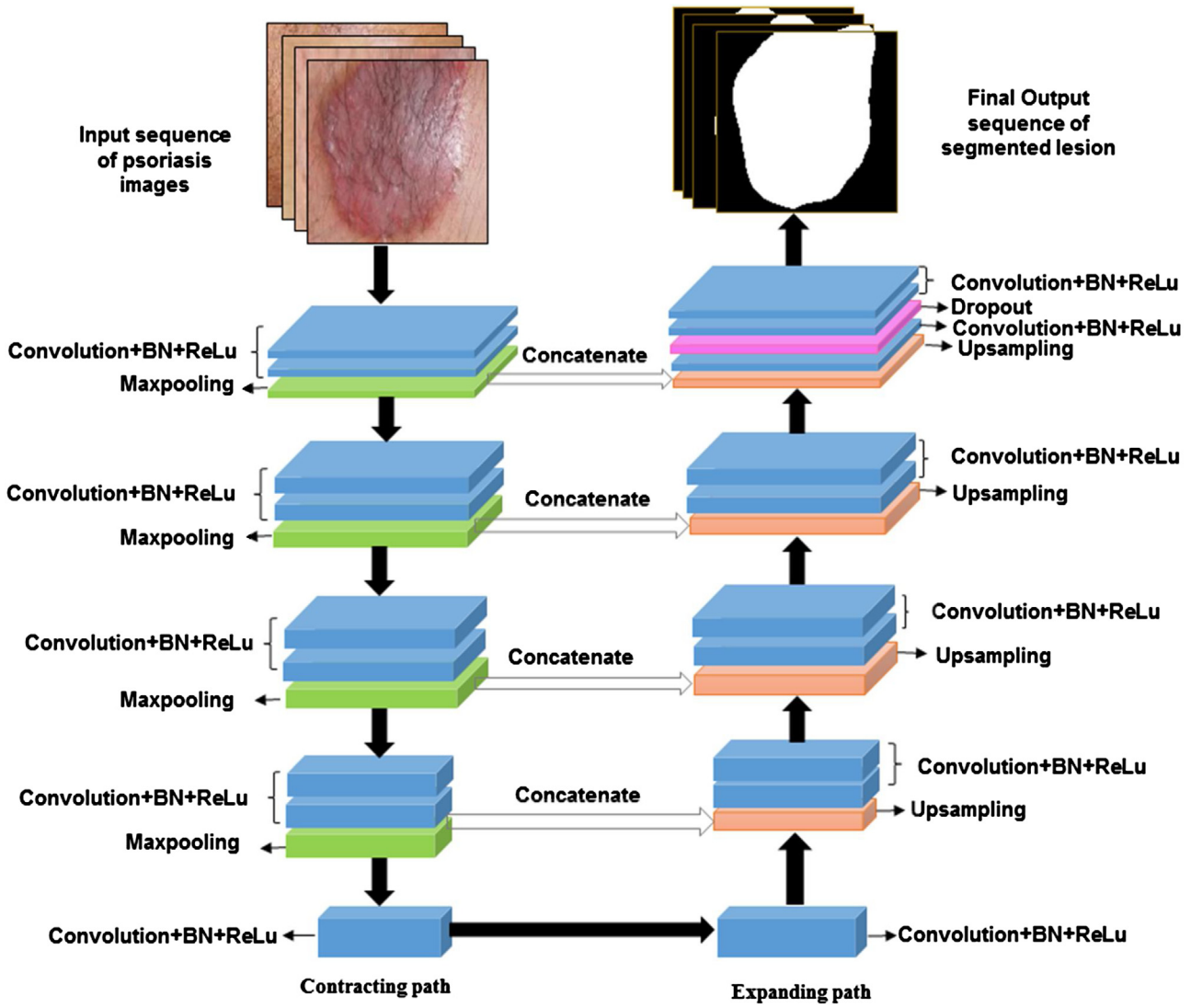


Fig. 3. Architecture of PsLSNet.

features. In the expanding path, upsampling is followed by 3×3 padded convolution, batch normalization, and the activation layer, implemented sequentially to achieve better segmentation outcomes. Here, both the contracting and expanding paths have similar parameters in terms of filter size and stride length. As explained

earlier, the U-Net architecture utilizes a convolutional operation at the output of the expanding path rather than using a fully connected layer, meaning that the U-Net model is well suited to pixel-wise classification. A detailed explanation of each layer is presented in the following.

Table 1
Architectural details of the PsLSNet.

Contracting path				Expanding path			
L. N.	Layers in contracting path	Filter size	Output shape	L. N.	Layers in expanding path	Filter size	Output shape
L ₁	Input		(128,128,3)	L ₁₆	Upsampling-1 cat1=(conv8+up1)	2 × 2	(16,16,128) (16,16,192)
L ₂	Conv-1+BN + ReLU	3 × 3	(128,128,8)	L ₁₇	Conv11+ BN + ReLU	3 × 3	(16,16,64)
L ₃	Conv-2+ BN + ReLU	3 × 3	(128,128,8)	L ₁₈	Conv-12+ BN + ReLU	3 × 3	(16,16,64)
L ₄	Maxpool-1	2 × 2	(64,64,8)	L ₁₉	Upsampling-2 cat2=(Maxpool3+up2)	2 × 2	(32,32,64) (32,32,96)
L ₅	Conv-3+BN + ReLU	3 × 3	(64,64,16)	L ₂₀	Conv-13+ BN + ReLU	3 × 3	(32,32,32)
L ₆	Conv-4+BN + ReLU	3 × 3	(64,64,16)	L ₂₁	Conv-14+ BN + ReLU	3 × 3	(32,32,32)
L ₇	Maxpool-2	2 × 2	(32,32,16)	L ₂₂	Upsampling-3 cat3=(conv3+up3)	2 × 2	(64,64,32) (64,64,48)
L ₈	Conv-5+BN + ReLU	3 × 3	(32,32,32)	L ₂₃	Conv-15+ BN + ReLU	3 × 3	(64,64,16)
L ₉	Conv-6+BN + ReLU	3 × 3	(32,32,32)	L ₂₄	Conv-16+ BN + ReLU	3 × 3	(64,64,16)
L ₁₀	Maxpool-3	2 × 2	(16,16,32)	L ₂₅	Upsampling-4 cat4=(Maxpool1+up4)	2 × 2	(128,128,16) (128,128,24)
L ₁₁	Conv-7+BN + ReLU	3 × 3	(16,16,64)	L ₂₆	Conv-17+ BN + ReLU	3 × 3	(128,128,8)
L ₁₂	Conv-8+BN + ReLU	3 × 3	(16,16,64)	L ₂₇	Dropout (value = 0.5)		
L ₁₃	Maxpool-4	2 × 2	(8,8,64)	L ₂₈	Conv-18+ BN + ReLU	3 × 3	(128,128,8)
L ₁₄	Conv-9+BN + ReLU	3 × 3	(8,8,128)	L ₂₉	Output = Conv19+sigmod	1 × 1	(128,128,1)
L ₁₅	Conv-10+BN + ReLU	3 × 3	(8,8,128)				

Conv = convolution, BN = batch normalisation, ReLU = rectifier linear unit, cat = concatenation, L. N. = layer number, Maxpool = max pooling.

2.1.1. Convolution layer

A total of 19 convolution operations are performed together with the batch normalized input and the ReLU activation function. The first convolution layer is L₂, in which 2D convolution between an input image of size (128 × 128) and a filter of size 3 × 3 takes place. The mathematical representation of the 2D convolution operation is as follows:

$$C_{ij} = f \left(b_{ij} + \sum_{m=0}^{K-1} \sum_{n=0}^{K-1} (X_{i+m,j+n})^{BN} * W_{mn} \right) \quad (1)$$

where C_{ij} is the output of the convolution layer (1 ≤ i, j ≥ 128, the size of the input image), f(.) is the ReLU activation function,

X^{BN} is the batch normalised input, W_{mn} is the weight and b_{ij} is the bias.

Similarly, the convolution operations in the remaining 18 layers are performed using Eq. (1). Successive convolution is followed by max pooling in the contracting path to extract contextual information from the input mini-batches. A 1 × 1 convolutional filter is utilised at the output of the network in order to reach the filter map, with a depth of two classes (lesion and non-lesion).

2.1.2. Max-pooling layer

After getting the activation map of psoriasis lesion, the max-pooling operation has been performed at each step of convolution in contracting path. The max-pooling layer is utilized by U-Net model in order to extract the features having spatial invariance [30]. Spatial invariance features are obtained by down-sampling the incoming mini batches of data. The max-pooling operation is also beneficial to prevent overfitting problem. The size of max-pooling has been fixed as 2 × 2 in the contracting path of proposed method. The max-pooling operation performs maxima in each sub-windows of the input matrix and stores it in the corresponding output matrix. The output of the max-pooling operation can be expressed by the following Eq. (2).

$$P_{ij} = \max_{i,j}^{m,n} C_{ij} \quad (2)$$

where, C_{ij} is the output of the convolution layer, P_{ij} is the output of pooling layer.

2.1.3. Up-sampling

The U-Net model uses an upsampling layer in the expanding path. Global image features are extracted in the contracting path,

while local image features are extracted by utilizing successive upsampling operations in the expanding path. The main advantage of the upsampling operation is the reconstruction of the original size of activation and production of a dense activation map. An expanded, dense feature map can be produced by the process of upsampling and successive convolution operations, and this is helpful in achieving a better segmentation map at the output. The upsampling layer in the expanding path increases the image size, while in the contracting path, the downsampling operation allows the abstraction of features. When the downsampled features (dense features) have been concatenated with high-resolution (dense) features in the expanding path, consecutive convolution layers are utilized to learn and gather more accurate information. The expanding path utilizes upsampling followed by a convolutional layer, in order to retrieve the resolution lost during the max pooling operation on the input mini-batches of psoriasis data in the contracting path. The upsampling layer is followed by a convolutional operation in the expanding segment of the architecture, to retrieve the lost details of the image. The contracting segment of the architecture encodes the image information, while the expanding segment is responsible for capturing the local details present in the image (lesion details). The upsampling operation is obtained using a nearest neighbor resampling method based on an interpolation technique. The size of the input image is enlarged after performing the nearest neighbor technique on each pixel and its neighbor, as the algorithm simply creates copies of each pixel and places them at nearby locations.

2.1.4. Loss function

A loss function based on the Dice similarity coefficient (DSC) has been used extensively in medical image segmentation [31,32]. In this paper, we adopt a Dice-based loss function since this is unaffected by the data imbalance problem and produces good results compared to those of a weighted cross-entropy technique, which is difficult to optimize [33]. The DSC is used to assess the performance of the psoriasis lesion segmentation. To measure the overlap between the actual and predicted psoriasis lesion, we propose the DSC, as shown in Eq. (3):

$$DSC(P, Q) = \frac{2(P \cap Q)}{P + Q} \quad (3)$$

where P is the value predicted by the classifier and Q is the ground truth value. We adopt the binary cross entropy (BCE) based on the

Dice loss [34] as a loss function. The Dice loss function and BCE can be calculated by Eqs. (4–6):

$$D = 1 - \text{DSC} \quad (4)$$

$$L = \text{BCE} + (1 - D) \quad (5)$$

$$\text{BCE} = \sum_{n=1}^M (P * \log * Q) \quad (6)$$

where D is the Dice loss, L is the loss, M = 2 is the number of classes (the psoriasis lesion and non-psoriasis portions of the skin), P is the ground truth, and Q is the predicted output.

3. Experimental setup

Different experiments are performed for segmentation of psoriasis lesion using a PsLSNet architecture which includes the dataset with all classes (explained in section III (A)), individual class, good and challenging images, and only with challenging images. These experiments are implemented in Python using the Keras [35] deep learning library, with TensorFlow as a backend [36] and the OpenCV library [37] on an Intel Core i7, 2.20 GHz CPU, GeForce GTX 1060 GPU with 6 GB graphics memory.

3.1. Database preparation

We used a larger data set of 5179 images collected from 1026 psoriasis patients, with 459 females and 567 males. Based on the severity of psoriasis this dataset divided into three classes such as moderate, severe and very severe. These patients were selected irrespective of age, gender, level of severity or race. The psoriasis images were collected from the Psoriasis Clinic and Research Centre, Psoriatreat, Pune, Maharashtra, India, using a Sony NEX-5 with a 22 mm lens and 350 dpi in the presence and with the support of a dermatologist. The images were then processed in Joint Photographic Expert Group (JPEG) format with a color depth of 24 bits per pixel. The corresponding ground truths for 5241 images were prepared manually and verified by the dermatologist. Further, without much pre-processing, we simply resized the original image to 128×128 and employed a bilinear interpolation. The RGB image was scaled between zero and one. Out of 5241 images, 3625 images are used to train the model that includes images of different class and quality. Remaining 1554 images are used for testing in the first experiment. In the second experiment, 518 images of each class tested separately. In the third experiment, 1195 good images and 359 challenging images tested separately. In the final experiment, 62 most challenging images (see Fig. 1) are validated separately to analyze the generalization ability of the proposed model for unscented data (not included in training)

3.2. Training of U-Net

As discussed in the previous section, the proposed architecture utilizes 19 convolutional layers. At the outset, the weights are initialized using Xavier's method [38]; later, the hyper parameters are fine-tuned to improve the performance of the implemented psoriasis lesion segmentation model. The details of the training of U-Net are explained in the following.

3.2.1. Stochastic optimization using Adam

Adam is a method for stochastic gradient descent (SGD) optimization in machine learning. We used the Adam (adaptive moments) optimizer in our proposed method as it has many advantages [39] over classical gradient descent methods; The learning rate is a critical hyper parameter that has a significant effect on training accuracy, and the selection of an effective learning rate

for a specific application is very challenging. In order to choose a learning rate, we utilize an adaptive learning-rate-based strategy in which the learning rate can vary during the training process. We set the initial learning rate to 0.003 to speed up the training process in this experiment. If the training metric (validation loss) of the deep learning model stagnates during the training process, there is a benefit to reducing the learning rate by some predefined factor. In our proposed method, we employ a strategy based on a learning rate scheduler to make the learning rate adaptive. The learning rate scheduler call-back is utilized to monitor whether there is any major improvement in the accuracy during the training process; if the metric of the training process stagnates over a certain number of iterations during training, then the learning rate scheduler reduces the learning rate by a predefined factor.

3.2.2. Batch normalization

In this study, we use batch normalization to reduce the internal covariant shift in both the contracting and expanding paths. Due to the changes in the network parameters during a training session, there will be a change in the distribution of activation of the network, and this is defined as the internal covariant shift [40]. Suppose we have a mini-batch of psoriasis data. Since there are different activation maps in each layer, in both the contracting and expanding paths, each activation map undergoes the batch normalization process independently. A normalized mini-batch is defined as N and given by Eq. (8):

$$\text{Mini-batch}(b) = \{x_1, x_2, \dots, x_n\} \quad (7)$$

$$\text{Normalized mini-batch}(N) = \frac{x_i - \bar{x}_b}{\sqrt{\sigma_b^2 + \varepsilon}} \quad (8)$$

$$\text{Mean of the mini-batch}(\bar{x}_b) = \frac{1}{n} \sum_{i=1}^n x_i \quad (9)$$

$$\text{The variance of the mini-batch}(\sigma_b^2) = \frac{1}{n} \sum_{i=1}^n (x_i - \bar{x}_b)^2 \quad (10)$$

where x is the input activation for a mini-batch b , and n is the total number of psoriasis samples for a particular mini-batch.

3.2.3. Dropout

The deep convolutional network is a powerful technique for classification and segmentation tasks, but such networks are prone to the problem of overfitting. We, therefore, use dropout [41] in our proposed architecture to reduce this overfitting. In this process, the output of each neuron in a given layer is assigned to zero with probability p , thus discarding the involvement of those specific dropout neurons from both forward and backward propagation. For each mini-batch of data, a subset of these disabled neurons is drawn, hence producing a different architecture. For each of these different architectures, the dropout technique utilizes the ensemble method to train all sub-networks in one epoch, meaning that a particular neuron cannot depend on the existence of another specific neuron, and hence the learning model is forced to learn the robust features that are essential within different subsets. In this study, the dropout layer is applied at the L_{27} and L_{28} layers of the modified U-Net architecture (see Table 1) and the dropout probability (p) is set to 0.5.

3.2.4. Post processing

The output of the U-Net model is a subsequent probability map. In the lesion probability map, each pixel represents the probability of whether the particular pixel belongs to the psoriasis lesion or the surrounding skin. After obtaining the probability map, we employ thresholding to obtain a binary mask for further evaluation of the

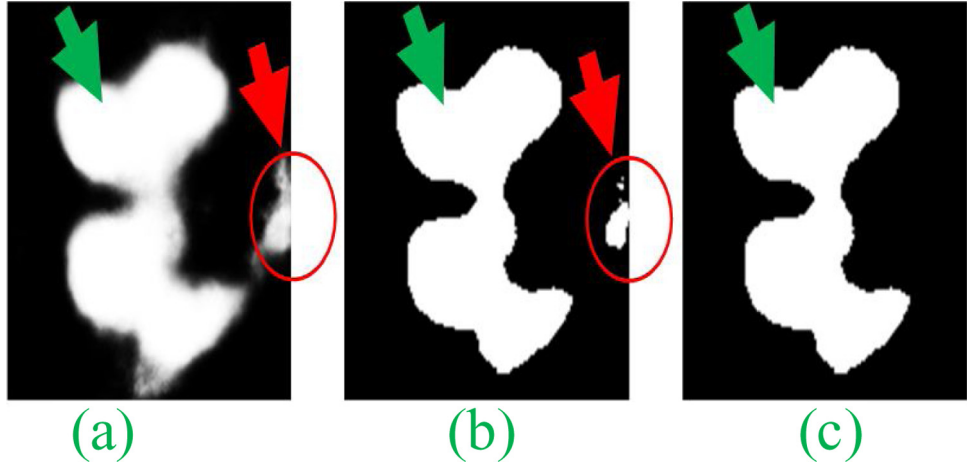


Fig. 4. Removing minor artifacts: (a) probability map; (b) result of thresholding; (c) final output after removing the false lesion. The green arrow indicates the true psoriasis lesion, and the red arrow indicates false detection due to artifacts.

proposed method. We fix a higher threshold value ($th = 0.8$), which gives an optimal binary mask after observing and analyzing the probability maps. The thresholding condition is given by Eq. (11):

$$\text{Output} = \begin{cases} 1, & \text{if pixel value} \geq th \\ 0, & \text{else} \end{cases} \quad (11)$$

We observe that the number of pixels contained within the lesion (psoriasis) is greater than the number contained in the false lesion (artifacts). Further images with multiple connected components are selected and the area has been calculated for each connected component. After calculating the area for each labeled connected component, the smaller area components are eliminated based on a pre-threshold value of 600. Fig. 4 shows the output of post processing.

4. Results

In order to measure the performance of the proposed segmentation method, we compare the ground truth mask, as verified by the dermatologist, with the mask generated by the proposed method. The effectiveness of the proposed U-Net-based psoriasis lesion segmentation technique is evaluated in this section. We quantify the result using four different indices (Dice coefficient, sensitivity, specificity, and accuracy) in comparison with the ground truth to examine the performance of the proposed method. The accuracy defines the proficiency of separating the lesion and skin properly, while the sensitivity and specificity represent the efficiency of lesion and skin segmentation independently. The formulae for these performance indices are given in Eqs. (12)–(16):

$$\text{Dice coefficient (DSC)} = \frac{2TP}{2TP + Fn + Fp} \quad (12)$$

$$\text{Accuracy (ACC)} = \frac{Tp + Tn}{Tp + Tn + Fp + Fn} \quad (13)$$

$$\text{Jaccard index (JI)} = \frac{Tp}{Tp + Fp + Fn} \quad (14)$$

$$\text{Sensitivity (SE)} = \frac{Tp}{Tp + Fn} \quad (15)$$

$$\text{Specificity (SP)} = \frac{Tn}{Tn + Fp} \quad (16)$$

where Tp =True positive, Tn =True negative, Fp =False positive, and Fn =False negative

The values of the different metrics were evaluated for the dataset of 1554 psoriasis images and are shown in Table 2. We

Table 2
Performance evaluation metrics (in percentages).

ACC	DSC	JI	SE	SP
94.80	93.03	86.40	89.60	97.60

obtained a Dice coefficient of 93.03% and Jaccard index of 86.40%, where the latter represents the similarity between the segmented lesion and the ground truth. The accuracy of 94.80% shows the consistency of our proposed method. Moreover, we are able to differentiate between the skin and lesion effectively, as demonstrated by the values of sensitivity (89.60%) and specificity (97.60%). A graph of the Dice coefficient with the iteration number is given in Fig. 5 and shows that the DSC in the training and validation phases are almost identical to each other between iterations 0 to 23. The value of DSC for validation improves from 0.65 to 0.92 over 47 iterations and then fluctuates between 0.92 and 0.93 for the remaining iterations.

In Fig. 6, we show the results of psoriasis segmentation for the validation dataset, in which the red contour represents the ground truth of psoriasis lesion, as identified by an expert, and the green contour represents the segmentation output of the proposed method. The results of the proposed method clearly show that the trained model is capable of differentiating between a lesion and normal skin.

Furthermore, the effect of the inclusion of more challenging images on the performance of the proposed model was examined by performing experiments with and without these challenging images. Note that the same training model was used in these experiments. In our first experiment, the validation dataset was separated into three different classes: very severe, severe and moderate. We compared the performance of class-wise psoriasis segmentation, and it can be observed from Table 3 that the moderate class provided the highest performance in terms of DSC, JI, and SE. The texture of the moderate class was consistent, with proper lesion boundaries, unlike the severe and very severe classes, which contained challenging images with various artifacts, giving lower performance metrics for these classes. The corresponding results are shown in Table 3.

In the second experiment, we separated all the good-quality images from the more challenging ones. In this experiment, we evaluated the segmentation performance of the proposed model on some of the challenging images in the validation dataset. To check the performance, we considered only images with optimal and suboptimal results, with the aim of observing the effects of

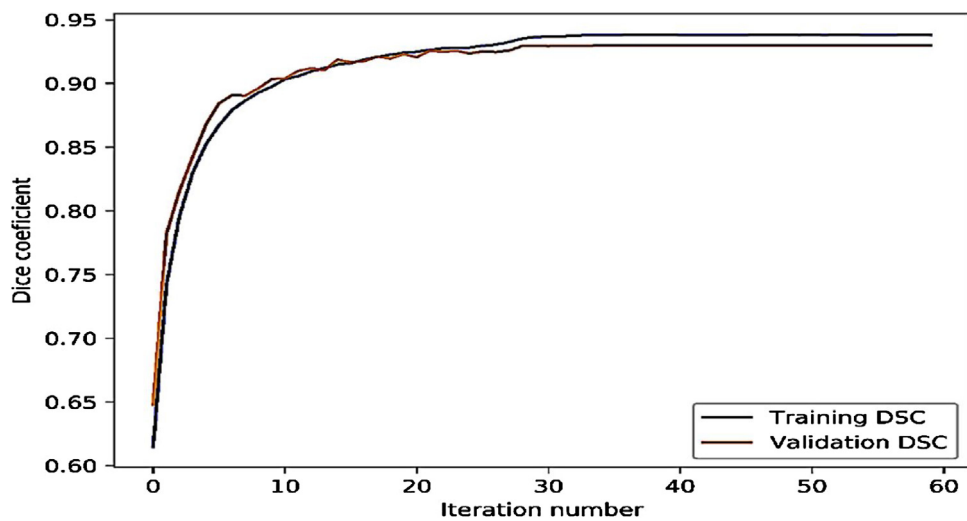


Fig. 5. DSC plot for training and validation.

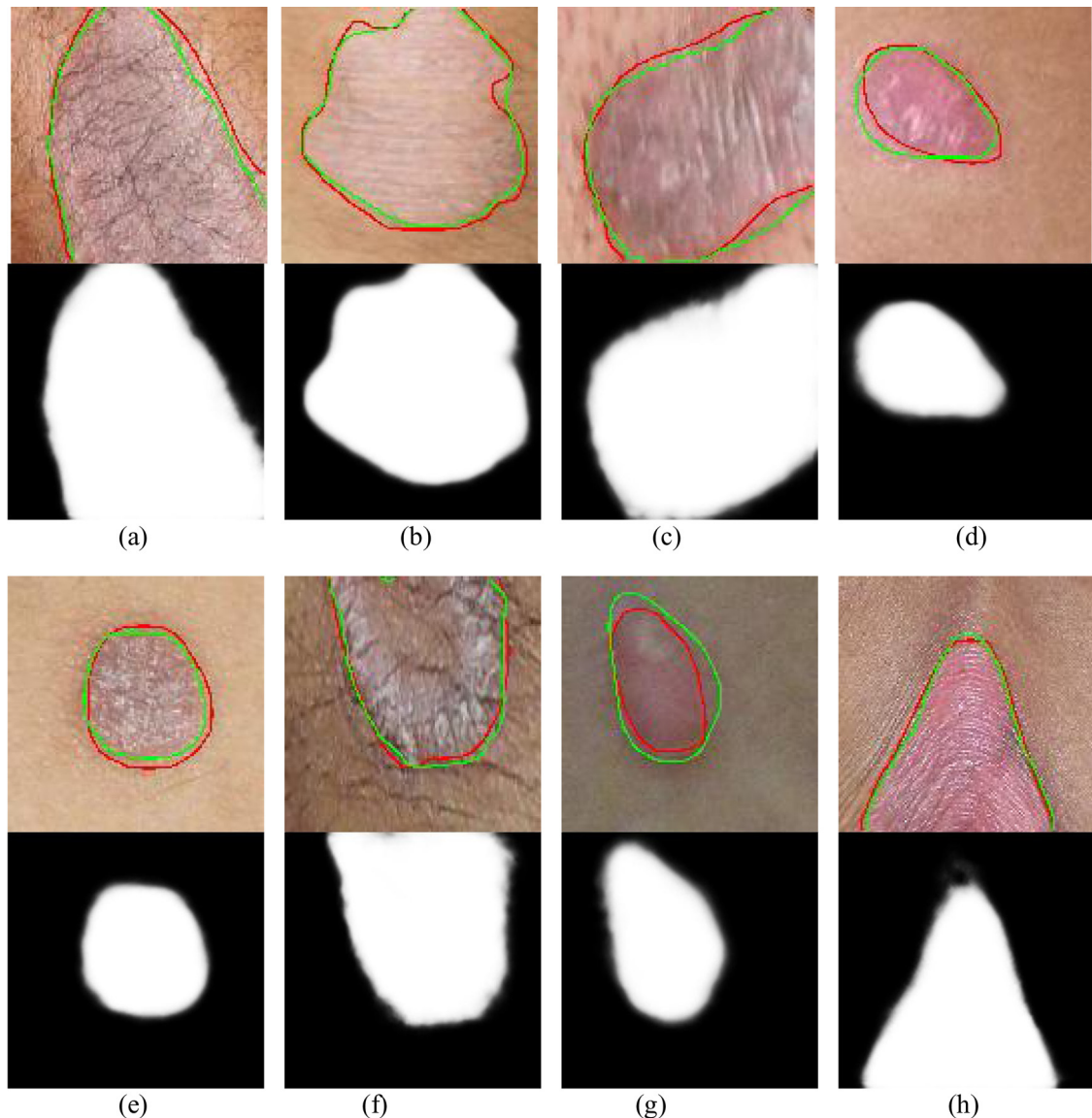


Fig. 6. The samples of the results of psoriasis skin lesion segmentation. The results of automated segmentation and ground truth are shown by the green and red contours, respectively. The first and third rows are the original RGB testing images, and the second and fourth rows are the corresponding probability maps generated by the proposed method.

Table 3

Performance evaluation of class-wise psoriasis lesion detection.

Psoriasis class	ACC	DSC	Jl	SE	SP
Very severe	0.9582	0.9370	0.8834	0.9054	0.9845
Severe	0.9587	0.9377	0.8863	0.9072	0.9848
Moderate	0.9574	0.9394	0.8885	0.9110	0.9821

Table 4

Performance evaluation of psoriasis segmentation for good-quality and challenging images.

Psoriasis data	ACC	DSC	Jl	SE	SP
Challenging images	0.91	0.90	0.80	0.84	0.96
Good-quality images	0.95	0.93	0.88	0.91	0.98

Table 5

Performance evaluation of lesion detection for the most challenging psoriasis images.

Psoriasis data	ACC	DSC	Jl	SE	SP
Challenging images	0.9233	0.8470	0.7297	0.7867	0.9739

these images on validation performance. The performance of the proposed model is summarised in [Table 4](#), which shows that with the inclusion of more challenging images, the loss function is not reduced further, and the Dice coefficient for the proposed method remains almost unchanged after several epochs.

Finally, we examined the performance of our proposed model using some of the most challenging images with very poor resolution, which were not included in our original validation dataset. The results of this experiment are shown in [Table 5](#). The results in [Tables 3 and 4](#) show that the main reason for the limit on the Dice coefficient of 0.9303 is due to the effect of the challenging images; although this result is greatly improved over those of other existing approaches, the problem still persists.

5. Discussion

In this section, we discuss the other key performance parameters, such as the reliability index, the segmentation results of some challenging cases, the selection of the optimizer and a comparative analysis between the proposed and the existing approaches for psoriasis lesion segmentation. We analyze the different hyperparameters to determine which provides the optimum segmentation metric, prior to selecting the final model. In this validation, the proposed model is evaluated using several different parameters, such as an optimizer and a reliability index. A similar model architecture and cross-validation technique are utilized in each experiment, while these parameters are altered.

5.1. Reliability index

In order to evaluate the reliability of our proposed method, we split the original data into 20%, 40%, 60%, 80%, and 100%. After splitting the dataset, the mean accuracy and standard deviation for each split of data were calculated. As discussed above, the same architecture and hyperparameters were used while varying the data size. The reliability index is defined by Eq. (17):

$$\tau_M = \left(1 - \frac{\sigma_M}{\mu_M}\right) \times 100 \quad (17)$$

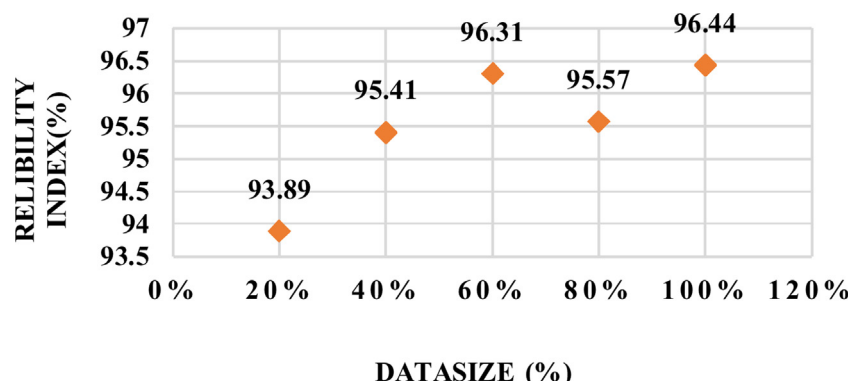
where M = split of original psoriasis data in percentage, τ_M = reliability index, σ_M = standard deviation of data, and μ_M = mean of data.

The reliability index for each 20% of the data sample is considered and the highest reliability index of 96.44% was found for the 100% data sample. This index represents the consistency of a particular model with an increment in the size of the dataset. We conducted the experiment using five sets of data, containing 1035, 2071, 3107, 4143 and 5241 psoriasis images, respectively. The corresponding graph is shown in [Fig. 7](#), which illustrates the consistency of the proposed model for various data sizes.

5.2. Effect of artifacts

As mentioned above, the dataset was prepared by the manual cropping of lesions from various parts of full body images, containing various artifacts such as shadows, skin hairs, etc. As we can see from [Fig. 8](#), there are various types of challenging case: the first ([Fig. 8a](#)) shows hair artifacts, while the second shows a fuzzy boundary of a psoriasis lesion ([Fig. 8b](#)) and the third shows suboptimal results due to uneven contrast ([Fig. 8c](#)). Small artifacts may be detected erroneously as a lesion, and this type of noise artifact in RGB psoriasis images can cause under- or over-segmentation of a lesion. Although the proposed method is able to differentiate between the lesion and the surrounding skin, results are in some cases suboptimal, as shown in [Fig. 8c](#). In order to mitigate these challenges, we adopt a simple approach based on the connected component area. After obtaining the binary mask from the lesion probability map, the pixels are clustered into components and a unique label is then assigned to each connected component [42].

For the challenging cases of the psoriasis images shown in [Fig. 1](#), the corresponding segmentation results using FCN, SegNet, U-Net and proposed method are shown in [Fig. 9](#). These results demonstrate that our proposed model is able to segment the lesion accurately as compare to FCN, SegNet, and U-Net.

**Fig. 7.** Reliability index of the proposed methodology.

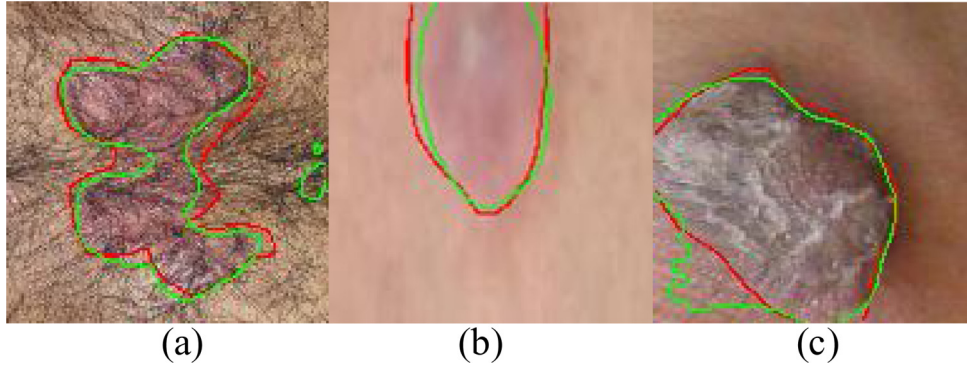


Fig. 8. Segmentation results for some challenging cases: (a) hair artifact; (b) fuzzy lesion boundary; and (c) suboptimal result due to uneven contrast.

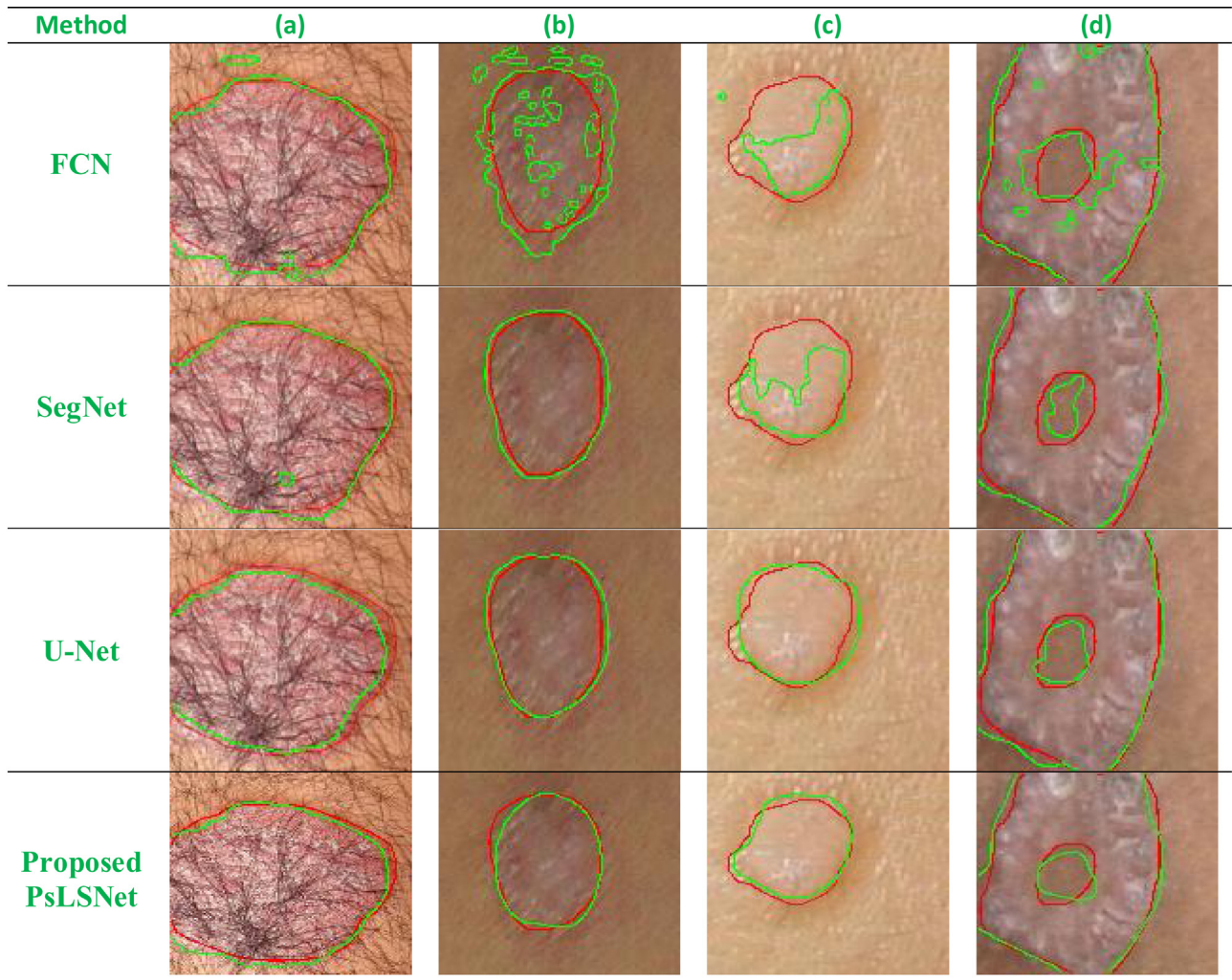


Fig. 9. Results of psoriasis lesion segmentation for some of the challenging images: (a) hair artifacts; (b) low contrast and a fuzzy boundary between the lesion and the surrounding skin; (c) very similar appearance of the psoriasis lesion and the surrounding skin; and (d) normal skin located in the middle of psoriasis lesion. The red contour indicates the skin lesions contoured by dermatologists, and the green contour indicates the result of the FCN, SegNet, U-Net and proposed method.

5.3. Adam vs SGD

We trained the same U-Net model with two different optimizers: the Adam optimizer and the SGD with Nesterov momentum. In both of these experiments, the learning rate was fixed at 0.003 and the momentum at 0.8. As training progressed, we observed

that the model with the Adam optimizer made rapid progress and converged faster, while SGD with Nesterov momentum was noisy and converged more slowly, as shown in Table 6. By analyzing the graph of epoch versus loss function, we can say that Adam is much more reliable than SGD. The table also confirms that the values for the validation matrices are significantly higher for Adam than for

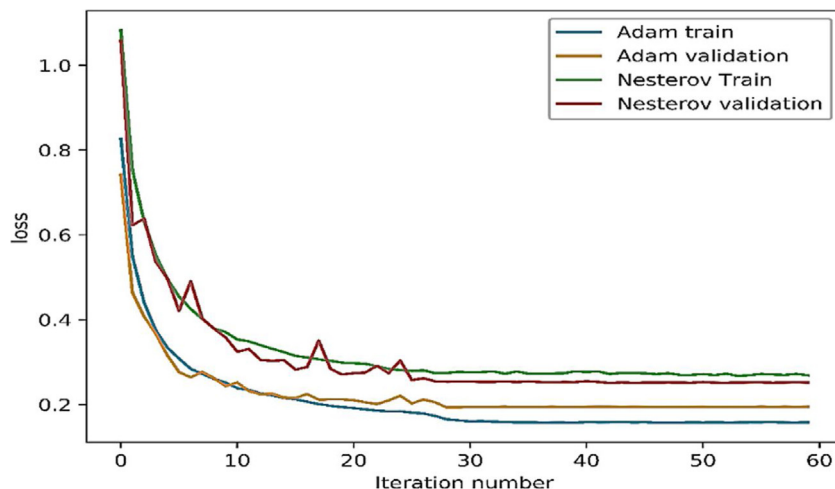


Fig. 10. Comparison between the Adam optimizer and SGD with Nesterov loss function for training and validation of the proposed model.

Table 6
Results for different optimization methods.

Optimizer	ACC	DSC	Jl	SE	SP
SGD + Nesterov	0.928	0.900	0.81	0.853	0.976
Adam	0.948	0.9303	0.864	0.896	0.976

SGD. A comparison between Adam and SGD with a Nesterov loss function for training and validation of the proposed model is shown in Fig. 10.

5.4. Comparative analysis between implemented and existing approaches for psoriasis lesion segmentation

To the best of our knowledge, no technique for psoriasis lesion segmentation using a deep learning approach has previously been reported. This may be due to a lack of a sufficiently large dataset of psoriasis images. We compare our proposed method of psoriasis lesion segmentation with existing techniques, as shown in Table 7. Existing techniques [10–12,14–16,19] are heavily dependent on features, and the results are validated using smaller datasets. A relatively large dataset of 5179 images is used in the present work, with automatic feature extraction employed to implement the segmentation task. The results of existing techniques have been evaluated using a single metric such as visual inspection [10,14,15] or accuracy [11–13]. Although the authors of [16] evaluated their results using the Dice coefficient, sensitivity, and specificity, the Dice coefficient was only 0.55, which is very low compared to that of the proposed method (DSC = 93.03). An improved DSC of 0.82 was reported in [19] for the extraction of 859 features. In our proposed

method, the results are validated using five different metrics, and we report improved values of DSC, JI and ACC for a larger dataset without the need for manual feature extraction.

As mentioned earlier, the U-Net version of FCN has been modified by introducing extra layers in the proposed PsLSNet based architecture. The appropriateness of PsLSNet in performing segmentation of psoriasis images has been compared with the classical FCN [43], SegNet [44] and U-Net [29]. Table 8 compares the performance of the proposed PsLSNet method with other techniques in terms of the performance indices and complexity (number of trainable parameters). It can be observed that the proposed PsLSNet method outperforms all the other methods in all performance indices. With regards to complexity, the proposed architecture is simpler as compared to SegNet and U-Net, but more computationally intensive to classical FCN.

The improved performance of U-Net architecture as compared to FCN and SegNet is attributed to the incorporation of larger number of feature channels in up sampling operation which allows the network to propagate the information to higher resolution layer. The ability of U-Net architecture in providing improved performance with low volume of training images [29]. Thus, it has been extensively utilized in various image segmentation task [45–48]. However for the present work of psoriasis image segmentation as reflected in Table 8, U-Net model suffers from the limitation of a larger number of trainable parameters leading to high computational cost and possible overfitting [41].

In this regard as detailed in Section (2), the original U-Net topology has been modified in the proposed PsLSNet architecture by exploiting batch normalization, pruning redundant layers and introducing new layers which contributes to the performance

Table 7
Comparative performance of the suggested model with existing works on psoriasis image segmentation.

Authors	Dataset	Data size	Features	Segmentation Technique	Performance Evaluation
Taur (2003) [10]	Psoriasis images	3	Texture	Neuro-fuzzy classifier	Visual validation
Taur et al. (2006) [11]	Psoriasis images	3	Texture	MSSC	ACC-0.91
Nidhal et al. (2010) [12]	Psoriasis and other diseases	24	Color and Texture	NN	ACC-0.83
Li-Hong et al. (2011) [13]	Psoriasis images	5	NA	K-means with morphological processing	ACC:91.58
Bogo et al. (2012) [14]	Psoriasis images	20	Color	Geometric Active Contours	Visual validation
Guoli et al. (2013) [15]	Psoriasis images	282	Color	GMM	Visual validation
Lu et al. (2013) [16]	Psoriasis images	103	Color and Texture	MRF + SVM	DSC:0.55 SE:0.81, SP:0.87
Shrivastav et al. (2017) [19]	Psoriasis images	670	HOS, Color, and Texture	Bayesian model	DSC:0.82, JI-0.71
Proposed Method	Psoriasis images	5241	Automated	Convolutional network	DSC:0.93, JI: 0.86, ACC:0.94 SE:0.89, SP:0.97

GMM-Gaussian Mixture Model, NN- Neural Network, MSSC-Multiresolution based Signature Subspace Classifier, SVM- Support Vector Machine, MRF-Markov Random Field, DSC-Dice Coefficient, JI = Jaccard Index, ACC = Accuracy, SE = Sensitivity, SP = Specificity, and HOS=Higher Order Statistics.

Table 8

Performance of different state of art deep learning architectures.

Architectures	ACC	DSC	JI	SE	SP	No. of Trainable Parameters
FCN	85.91	85.33	76.0	81.18	95.29	23161
SegNet	89.96	89.24	82.25	89.00	92.77	5463490
U-Net	93.34	92.98	86.00	89.43	95.87	34521281
Proposed PsLSNet	94.80	93.03	86.40	89.60	97.60	494081

enhancement. With PsLSNet improved performance is achieved in all the performance attributes with 70 times reduction in the trainable parameters as compared to U-Net. The effectiveness of the proposed approach in maintaining a trade-off between network complexity and overall performance is exhibited in Table 8.

6. Conclusion

In this paper, we propose an overall framework for a fully automated method of segmenting psoriasis lesion from RGB images. We implemented a modified U-Net-based architecture and adopted various training strategies to achieve an efficient training process and a reliably trained model. The proposed architecture is a modified fully convolutional network with fewer parameters than in the original U-Net topology. In this way, we attain accelerated training and very similar performance in terms of lesion segmentation with fewer layers and filters. In this study, we use batch normalization at each convolutional step to reduce the covariant shift and give faster training. A combined binary cross-entropy based Dice loss function is adopted since this directly increases the pixel-level accuracy and segmentation performance. The results of our experiments show that the proposed method is robust and segments lesions more accurately, even in challenging cases, than other existing approaches. In addition, our model is not only able to detect normal skin located in the middle of a psoriasis lesion but also lesions with a similar appearance to the surrounding skin. We also evaluated the reliability of the proposed method by calculating the reliability index for different sizes of datasets, demonstrating the consistency of the proposed method. We conducted several experiments to validate the effectiveness and generalisability of our trained model using some of the most challenging images. Finally, we compared the performance of our model with existing work, showing that our proposed method outperforms other existing feature-based learning methods. Further the PsLSNet can be utilized for the experimentation of psoriasis severity detection.

Conflict of interest statement

None declared.

Funding

The author(s) received no financial support for the research, authorship, and/or publication of this article.

Acknowledgments

The authors would like to thank the psoriasis patients who participated in this study.

References

- [1] C. Huerta, E. Rivero, L.A.G. Rodríguez, Incidence, and risk factors for psoriasis in the general population, *Arch. Dermatol.* 143 (12) (2007) 1559–1565.
- [2] H.M. Sander, L.F. Morris, C.M. Phillips, P.E. Harrison, A. Menter, The annual cost of psoriasis, *J. Am. Acad. Dermatol.* 28 (1993) 422–425.
- [3] B.A. Adam, Psoriasis in hospital population, *Med. J. Malay.* (June) (1980).
- [5] K.C. Yee, S.E. Choon, G.E. Khaw, R. Baba, S.H. Hussein, S.K. Ratti, Malaysian Patients Knowledge of Psoriasis: Psoriasis Association Members Vs Non-Members, *Persatuan Dermatologi, Malaysia*, 1999.
- [6] V.K. Shrivastava, N.D. Londhe, R.S. Sonawane, J.S. Suri, First review on psoriasis severity risk stratification: an engineering perspective, *Comput. Biol. Med.* 63 (2015) 52–63.
- [7] H.H. Roenigk, H.I. Maibach, Psoriasis, Marcel Dekker, in: C. Camisa (Ed.), *Handbook of Psoriasis*, second ed., Blackwell Publishing Ltd, UK, 1985, p. 2004.
- [8] T. Henseler, Genetics of psoriasis, *Arch. Dermatol. Res.* 290 (1998) 463–476.
- [9] S.R. Feldman, G.G. Krueger, Psoriasis assessment tools in clinical trials, *Ann. Rheum. Dis.* 64 (2) (2005) 65–68.
- [10] J.S. Taur, Neuro-Fuzzy approach to the segmentation of psoriasis images, *J. VLSI Signal Process. Syst. Signal Image Video Technol.* 35 (2003) 19–27.
- [11] J.S. Taur, G.H. Lee, C.W. Tao, C.C. Chen, C.W. Yang, Segmentation of psoriasis vulgaris images using multiresolution-based orthogonal subspace techniques, *IEEE Trans. Syst. Man Cybernet, Part B: Cybernet.* 36 (2) (2006) 390–402.
- [12] K.A. Nidhal, S.D. Nizar, A.A. Muhsin, R. Hind, Psoriasis detection using color and texture features, *J. Comput. Sci.* 6 (6) (2010) 648–652.
- [13] J. Li-Hong, W. Ming-Ni, Psoriasis image identification using k-means clustering with morphological processing, *Measurement* 44 (2011) 895–905.
- [14] F. Bogo, M. Samory, A. Belloni, Fortina, S. Piaserico, E. Peserico, Psoriasis segmentation through chromatic regions and geometric active contours, *International Conference of the IEEE EMBS* 28 (2012).
- [15] M. Guoli, H. Bei, Y. Wenming, S. Chang, Easy interactive and quick psoriasis lesion segmentation, in: *International Conference on Optical Instruments and Technology*, 2013, pp. 9045.
- [16] J. Lu, E. Kazmierczak, J.H. Manton, R. Sinclair, Automatic segmentation of scaling in 2-D psoriasis skin images, *IEEE Trans. Med. Imaging* 32 (4) (2013) 719–730.
- [17] V.K. Shrivastava, N.D. Londhe, Measurement of psoriasis area and severity index area score of indian psoriasis patients, *J. Med. Imaging Health Inf.* 5 (205) (2019) 1–8.
- [18] F. Xie, A.C. Bovik, Automatic segmentation of dermoscopy images using self Generating neural networks seeded by genetic algorithm, *Patt. Recogn.* 46 (2013) 1012–1019.
- [19] V.K. Shrivastava, N.D. Londhe, R.S. Sonawane, J.S. Suri, A novel and robust Bayesian approach for segmentation of psoriasis lesions and its risk stratification: inter-comparison of nine systems, *Comput. Methods Programs Biomed.* 150 (2017) 9–22.
- [20] Y. LeCun, Y. Bengio, G. Hinton, Review on deep learning, *Nature* 521 (2015) 436–444.
- [21] J. Ker, L. Wang, J. Rao, T. Lim, Deep learning applications in medical image analysis, *IEEE Access* 6 (2018) 9375–9389.
- [22] A.V. Mityakov, V.K. Varankin, Y.S. Tatarinov, Application of modern architectures of deep neural networks for solving practical problems, in: *IEEE International Conference on Soft Computing and Measurements (SCM)*, 2017.
- [23] S.S.M. Salehi, A. Gholipour, Auto-context convolutional neural network (Auto-net) for brain extraction in magnetic resonance imaging, *IEEE Trans. Med. Imaging* 36 (11) (2017) 2319–2330.
- [24] Y. Yuan, M. Chao, Y.C. Lo, Automatic skin lesion segmentation using deep fully convolutional networks with jaccard distance, *IEEE Trans. Med. Imaging* 36 (9) (2017) 01876–01886.
- [25] X. Li, H. Chen, X. Qi, Q. Dou, C. Fu, P.A. Heng, H-DenseUNet: hybrid densely connected UNet for liver and tumor segmentation from CT volumes, *IEEE Trans. Med. Imaging* (2018).
- [26] Novikov, D. Lenis, D. Major, J. Hladuvka, M. Wimmer, K. Buhler, Fully convolutional architectures for multi-class segmentation in chest radiographs, *IEEE Trans. Med. Imaging* (2018).
- [27] J. Long, E. Shelhamer, T. Darrell, Fully convolutional networks for semantic segmentation, *IEEE Trans. Pattern Anal. Mach. Intell.* 39 (4) (2017) 640–651.
- [28] Y. Yuan, M. Chao, Y.C. Lo, Automatic skin lesion segmentation using deep fully convolutional networks with jaccard distance, *IEEE Trans. Med. Imaging* 36 (9) (2017) 1876–1886.
- [29] Ronneberger, P. Fischer, T. Brox, U-net: convolutional networks for biomedical image segmentation, *International Conference on Medical Image Computing and Computer-Assisted Intervention MICCAI 2015* (2015) 234–241.
- [30] D. Scherer, A. Muller, S. Behnke, Evaluation of pooling operations in convolutional architectures for object recognition, in: *20th International Conference on Artificial Neural Networks (ICANN)*, 2010.

- [31] E. Gibson, W. Li, C. Sudre, L. Fidon, et al., Nifty net: a deep-learning platform for medical imaging, *Comput. Methods Programs Biomed.* 158 (2018) 113–122.
- [32] A. Novikov, D. Lenis, D. Major, Fully convolutional architectures for multiclass segmentation in chest radiographs, *IEEE Trans. Med. Imaging* 37 (8) (2018) 1865–1876.
- [33] S. Perone, E. Calabrese, J.C. Adad, Spinal cord gray matter segmentation using deep dilated convolutions, *Sci. Rep.* (2018).
- [34] M. Kheneda, V. Alexa, G. Krishnamurthia, Fully convolutional multi-scale residual DenseNets for cardiac segmentation and automated cardiac diagnosis using ensemble of classifiers, *Med. Image Anal.* (2018).
- [35] F. Chollet, Keras, "Keras: The Python Deep Learning library." [Online]. Available:, 2015 <https://keras.io/>.
- [36] M. Abadi, et al., TensorFlow: a system for large-scale machine learning, in: 12th USENIX Symposium on Operating Systems Design and Implementation (OSDI 16), 2016, pp. 265–283.
- [37] G. Bradski, The OpenCV Library, Dr. Dobb's J. Softw. Tools, 2000.
- [38] X. Glorot, Y. Bengio, "Understanding the difficulty of training deep feedforward neural networks, Proc. Aistats 9 (2010) 249–256.
- [39] L. Bottou, Stochastic Gradient Descent Tricks, *Neural Networks: Tricks of the Trade*, vol. 7700, Springer, 2012, pp. 421–436.
- [40] S. Ioffe, C. Szegedy, Batch normalization: accelerating deep network training by reducing internal covariant shift, *Mach. Learn.* 3 (2015) 448–456.
- [41] N. Srivastava, G. Hinton, A. Krizhevsky, L. Sutskever, R. Salakhutdinov, Dropout: a simple way to prevent neural networks from overfitting, *J. Mach. Learn. Res.* 15 (2014) 1929–1958.
- [42] R.C. Gonzalez, R.E. Woods, *Digital Image Processing*, 2008.
- [43] J. Long, E. Shelhamer, T. Darrell, Fully convolutional networks for semantic segmentation, in: Proceedings of the IEEE Conference on Computer Vision and Pattern Recognition, 2015.
- [44] V. Badrinarayanan, A. Handa, R. Cipolla, Segnet: a Deep Convolutional Encoder-decoder Architecture for Image Segmentation, *arXiv preprint: 1511.00561*, 2015.
- [45] X. Li, H. Chen, X. Qi, Q. Dou, C. Fu, P.A. Heng, H-DenseUNet: hybrid densely connected UNet for liver and tumor segmentation from CT volumes, *IEEE Trans. Med. Imaging* (2018).
- [46] H. Fu, J. Cheng, Y. Xu, D.W.K. Wong, Joint Optic Disc and Cup Segmentation Based on Multi Label Deep Network and Polar Transformation, *arXiv preprint: 1801.00926*, 2018.
- [47] G.M. Venkatesh, A Deep Residual Architecture for Skin Lesion Segmentation, *OR 2.0 Context- Aware Operating Theaters, Computer Assisted Robotic Endoscopy, Clinical Image-Based Procedures, and Skin Image Analysis*, Springer, Cham, 2018, pp. 277–284.
- [48] B. Jimmy, R. Caruana, Do deep nets really need to be deep, *Adv. Neural Inf. Process. Syst.* (2014).